SCIEPublish

Article

Effect of Support Preparation Method on the Performance of Ni/$SrTiO_3$ Catalysts for Dry Reforming of Methane

Tao Yang [1], Haoran Sun [1], Jingyi Yang [2], Ningyu Jia [1] and Meng Zhang [1,*]

[1] College of Chemistry, Zhengzhou University, Zhengzhou 450001, China; ytzs0214@163.com (T.Y.); sunhaoran123@gs.zzu.edu.cn (H.S.); jny15836562873@163.com (N.J.)

[2] School of Chemical Engineering, Zhengzhou University, Zhengzhou 450001, China; a1358852@163.com (J.Y.)

* Corresponding author. E-mail: zhangmeng1991@zzu.edu.cn (M.Z.)

Received: 27 October 2025; Revised: 6 November 2025; Accepted: 17 November 2025; Available online: 21 November 2025

ABSTRACT: Dry reforming of methane (DRM) offers an efficient route to simultaneously convert CH_4 and CO_2 into synthesis gas (H_2/CO), a key intermediate to produce fuels and valuable chemicals. Ni-based catalysts are regarded as the most promising candidates due to their high activity and low cost; however, their stability remains a major obstacle under the DRM conditions. Perovskite-type oxides such as $SrTiO_3$ possess high thermal stability, tunable composition, and strong metal-support interactions, making them ideal to enhance the dispersion and durability of Ni species. In this study, Ni/$SrTiO_3$ catalysts were synthesized via co-precipitation (CP), hydrothermal (HT), and sol-gel (SG) methods, and were comprehensively characterized before and after the reaction. The characterizations revealed that all samples preserved the perovskite framework after reduction and reaction. Among them, Ni/HT-STO and Ni/SG-STO exhibited larger surface areas (18.8 and 13.9 $m^2 \cdot g^{-1}$) and higher initial CH_4 conversions (66.3% and 68.9%) than Ni/CP-STO (44.8%). However, Ni/HT-STO underwent rapid deactivation, with CH_4 conversion decreasing to 21.2% after 60 h due to severe carbon accumulation (12.4 wt%) and notable Ni particle growth. In contrast, the sol-gel derived Ni/SG-STO maintained a higher activity (25.6% after 60 h) with moderate carbon deposition (9.2 wt%) and showed the smallest Ni particle growth of only 2.64 nm (from 14.91 to 17.55 nm), compared with 4.29 nm for Ni/CP-STO (25.83 to 30.12 nm) and 6.08 nm for Ni/HT-STO (27.12 to 33.20 nm). Temperature-programmed surface reaction (TPSR) analysis further revealed that Ni/SG-STO exhibited a more balanced CH_4 activation and CO_2 dissociation, enabling efficient carbon-oxygen coupling and inhibiting graphitic carbon formation. Overall, these results demonstrate that the sol-gel method effectively enhances the anti-sintering and anti-coking performance of Ni/$SrTiO_3$ catalysts.

Keywords: Dry reforming; $SrTiO_3$; Ni; Carbon deposition; Preparation method; Sintering resistance

1. Introduction

With the increasing depletion of fossil fuels and the growing concerns over global warming, developing efficient strategies for carbon resource utilization has become an urgent task for sustainable energy conversion [1–3]. Among various CO_2 mitigation and carbon recycling routes, dry reforming of methane (DRM) has attracted considerable attention because it simultaneously consumes two major greenhouse gases, CH_4 and CO_2, to produce synthesis gas (H_2/CO), which serves as a versatile feedstock to produce fuels and valuable chemicals [4–6]. The generated syngas can be further converted into higher hydrocarbons, alcohols, and aromatics through Fischer-Tropsch synthesis and related processes, providing a promising pathway for achieving carbon neutrality and reducing greenhouse gas emissions [7–9]. Ni-based catalysts are widely regarded as the most promising candidates for the DRM reaction due to their high catalytic activity and relatively low cost compared with noble metal catalysts such as Rh, Ru, and Pt. However, these catalysts still suffer from severe sintering and carbon deposition under high-temperature DRM conditions, which lead to rapid deactivation and hinder their long-term industrial application [10–12]. Therefore, designing catalysts that simultaneously exhibit high activity, strong sintering resistance, and excellent anti-coking capability remains a central challenge in DRM catalysis.

DRM reaction involves the concurrent activation of both CH_4 and CO_2 molecules on the catalyst surface [13]. CH_4 dissociation primarily occurs on the active Ni sites, generating surface carbon species that are prone to accumulate and

https://doi.org/10.70322/gct.2025.10021

form filamentous carbon. In contrast, CO_2 activation and oxygen mobility are mainly governed by the physicochemical properties of the support, which determine the ability to remove surface carbon via oxidation [14–16]. Consequently, support plays a critical role in enhancing the coking resistance and stability of Ni-based catalysts.

Among various support materials, perovskite-type oxides with an ABO_3 structure have gained increasing attention as catalyst supports owing to their excellent thermal stability, flexible composition, and high lattice-oxygen mobility [17–20]. These characteristics enable strong metal-support interactions and tunable redox properties that are highly favorable for improving metal dispersion and catalytic stability. Han et al. [21] reported that oxygen vacancy rich $Ni/SrTiO_{3-x}$ catalysts exhibited greatly enhanced CO_2 adsorption and activation, achieving nearly sixfold higher CO_2 conversion under photothermal conditions than stoichiometric $Ni/SrTiO_3$, owing to the synergistic interaction between Ni clusters and lattice vacancies. Luo et al. [22] demonstrated that $Ru/SrTiO_3$ nanosheets exposing {110} Sr-O-Ti facets could strongly anchor CO_2 and CO intermediates at the metal oxide interface, resulting in doubled CH_4 formation rates while maintaining nearly 100% selectivity under mild photothermal hydrogenation conditions. Cao et al. [23] further showed that La_2NiO_4 perovskite oxides acted as self-regenerative supports that decomposed *in situ* to yield finely dispersed Ni^0 nanoparticles strongly bound to La_2O_3, which exhibited high activity, excellent coking resistance, and stable performance after repeated regeneration cycles.

The preparation method has a significant influence on the structural and physicochemical properties of catalysts, thereby strongly affecting their catalytic performance. Pirzadi et al. [24] reported that, among five $Ni/CaO{\cdot}Al_2O_3$ catalysts synthesized by different methods, the one obtained via the sol-gel route exhibited the highest DRM activity, which was attributed to its finely dispersed Ni particles and enhanced metal-support interaction. Cao et al. [25] compared $LaNiO_3$ perovskite catalysts prepared by sol-gel, co-precipitation, and hydrothermal methods, and found that the sol-gel derived sample showed the highest activity and stability due to its improved crystallinity and lower impurity content. Similarly, Suárez-Vázquez et al. [26] synthesized $SrTiO_3$ perovskites via a one-pot hydrothermal route, which yielded dendritic structures with higher surface areas and richer surface oxygen species, resulting in significantly enhanced oxidation activity and stability. Moreover, Sunny et al. [27] employed a hydrothermal strategy to prepare MOF-74/$SrTiO_3$ composites with controlled crystal growth and improved structural stability, further highlighting the crucial role of the synthesis route in tuning the physicochemical characteristics of $SrTiO_3$-based materials.

Despite these advances, systematic investigations comparing the influence of different preparation methods on the metal-support interaction and reaction behavior of perovskite-derived $Ni/SrTiO_3$ catalysts remain limited. In this work, $Ni/SrTiO_3$ catalysts were synthesized via co-precipitation (CP), hydrothermal (HT), and sol-gel (SG) methods. Their catalytic performances in the DRM reaction were evaluated in a fixed-bed reactor, and comprehensive structural characterizations were conducted before and after the reaction to elucidate the relationship between synthesis route, metal-support interaction, and catalytic stability. Furthermore, temperature-programmed surface reaction (TPSR) experiments were performed by sequentially introducing CH_4, CO_2, and CH_4/CO_2 mixtures to gain a deeper insight into the surface reaction behavior and carbon oxygen coupling mechanism during DRM.

2. Materials and Methods

2.1. Materials

$Ni(NO_3)_2{\cdot}6H_2O$ (98%) and $Sr(NO_3)_2$ (98%) were purchased from Macklin Biochemical Technology Co., Ltd. (Shanghai, China). $Ti(OC_4H_9)_4$ (99%), EDTA, and citric acid were obtained from Aladdin Biochemical Technology Co., Ltd. (Shanghai, China). All chemicals were of analytical grade and used as received.

2.2. Preparation Method

2.2.1. Preparation of $SrTiO_3$ Support

$SrTiO_3$ (STO) supports were prepared by CP, HT, and SG methods. The Sr/Ti molar ratio was fixed at 1:1.

- CP method: Titanium butoxide ($Ti(OBu)_4$) was gradually added to the strontium nitrate ($Sr(NO_3)_2$) solution under continuous stirring at 350 rpm to ensure homogeneous mixing. Subsequently, adjust the pH to around 9 by $NH_3{\cdot}H_2O$. and continue stirring at 40 °C for 4 h to complete the precipitation. The resulting precipitate was concentrated by rotary evaporation at 60 °C, dried overnight at 120 °C, pre-calcined at 400 °C for 4 h, and finally calcined at 700 °C for 4 h.
- HT method: Strontium nitrate ($Sr(NO_3)_2$) was dissolved in 60 mL 0.2 M NaOH solution, and titanium butoxide ($Ti(OBu)_4$) was gradually added under stirring. The mixture was transferred into a 100 mL Teflon-lined and

hydrothermally treated at 180 °C for 24 h. The resulting solid was washed several times with deionized water until it reached neutral pH, and then dried overnight at 120 °C. Finally, the dried powder was calcined at 400 °C for 4 h and 700 °C for another 4 h.

- SG method: Strontium nitrate ($Sr(NO_3)_2$) was dissolved in deionized water, while titanium butoxide ($Ti(OBu)_4$) was separately dissolved in ethanol. EDTA and citric acid (CA) were added to the $Sr(NO_3)_2$ solution, and the pH was adjusted to 7–8 using $NH_3 \cdot H_2O$. The $Ti(OBu)_4$ solution was then slowly added to the mixed solution under continuous stirring and heated at 100 °C until a gel was formed. The obtained gel was dried overnight at 120 °C, pre-calcined at 400 °C for 4 h to remove organic residues, and finally calcined at 700 °C for 4 h.

2.2.2. Preparation of $Ni/SrTiO_3$ Catalysts

In this work, $Ni/SrTiO_3$ catalysts were prepared by the impregnation method with a nominal Ni loading of 5 wt%. Nickel nitrate hexahydrate ($Ni(NO_3)_2 \cdot 6H_2O$) was dissolved in deionized water to form a 0.5 $mol \cdot L^{-1}$ solution, which was then mixed with $SrTiO_3$ supports prepared by the CO, HT, and SG methods. The mixtures were rotary-evaporated at 40 °C to remove excess water, dried overnight at 120 °C, and calcined sequentially at 400 °C for 4 h and 700 °C for 4 h. The resulting catalysts were denoted as Ni/CP-STO, Ni/HT-STO, and Ni/SG-STO.

2.3. Characterization

The phase composition of the samples was analyzed by X-ray diffraction (XRD, Rigaku Ultima IV， Rigaku Corp., Tokyo, Japan, Cu Kα, λ = 1.5406 Å). The surface area and pore structure were determined by N_2 adsorption-desorption isotherms at −196 °C using a Micromeritics ASAP 2460 analyzer (Micromeritics Instrument Corp., Norcross, GA, USA). The morphology and particle distribution were observed by transmission electron microscopy (TEM, JEOL JEM-2100F, JEOL Ltd., Tokyo, Japan). The reducibility of the catalysts was evaluated by H_2 temperature-programmed reduction (H_2-TPR, Micromeritics AutoChem II 2920, Micromeritics Instrument Corp., Norcross, GA, USA). For H_2-TPR, The U-type quartz reactor was loaded with 200 mg of catalyst and pretreated under Ar (50 mL/min) at 300 °C for 60 min. Subsequently, the reactor was cooled to 100 °C, and a 10% H_2/Ar mixture gas (30 mL/min) was introduced, while the temperature increased to 850 °C (10 °C/min). The thermal conductivity detector (TCD) was utilized to detect the H_2 consumption signals. For H_2 chemisorption, the catalyst (100 mg) was first reduced under a flow of 10% H_2/Ar (30 $mL \cdot min^{-1}$) at 700 °C for 60 min, followed by purging with Ar (30 $mL \cdot min^{-1}$) to remove the residual H_2. The reactor was then cooled down to 50 °C under Ar flow, and pulses of H_2 were introduced until saturated adsorption was achieved. Assuming an adsorption stoichiometry of H/Ni = 1, the Ni dispersion was subsequently calculated. Thermogravimetric analysis (TGA) of the spent catalysts was performed on Netzsch STA 2500 (Netzsch-Gerätebau GmbH, Selb, Germany). The samples were heated from 30 °C to 850 °C at a rate of 10 °C/min under air, and the TG curves were recorded. The DTG profile was the first-order differential of the corresponding TG curve.

2.4. Catalytic Activity Evaluation

The catalytic performance of the $Ni/SrTiO_3$ catalysts was evaluated in a quartz fixed-bed tubular reactor (inner diameter: 6 mm). The catalyst (200 mg, 20–40 mesh) was diluted with quartz sand (1000 mg, 20–40 mesh) and placed at the center of the reactor. Prior to the reaction, 10% H_2/Ar (30 $mL \cdot min^{-1}$) was introduced to reduce the catalyst at 700 °C for 60 min. Subsequently, a mixture of gases CH_4 and CO_2 was introduced into the reactor with a CH_4/CO_2 ratio of 1:1 (*v*/*v*) and a total flow rate of 80 $mL \cdot min^{-1}$, corresponding to a weight hourly space velocity (WHSV) of 24,000 $mL \cdot g^{-1} \cdot h^{-1}$. Finally, the outlet gases were analyzed by an online gas chromatograph (GC, equipped with a TDX-01 column and TCD).

The conversions of CH_4 and CO_2 and the molar ratio of H_2/CO were calculated by Equations (1)–(3):

$$CH_4 \text{ conversion } (\%) = \frac{F_{in,CH_4} - F_{out,CH_4}}{F_{in,CH_4}} \times 100\% \quad (1)$$

$$CO_2 \text{ conversion } (\%) = \frac{F_{in,CO_2} - F_{out,CO_2}}{F_{in,CO_2}} \times 100\% \quad (2)$$

$$H_2/CO\ ratio = \frac{F_{out,H_2}}{F_{out,CO}} \quad (3)$$

where, F_{in,CH_4} and F_{in,CO_2} were the flow rate ($mL \cdot h^{-1}$) of CH_4 and CO_2, respectively, at the inlet; F_{out,CH_4}, F_{out,CO_2}, F_{out,H_2} and $F_{out,CO}$ were the flow rate ($mL \cdot h^{-1}$) of CH_4, CO_2, H_2 and CO, respectively, at the outlet.

CO and coke selectivity were calculated based on the overall carbon balance according to the following Equations (4) and (5):

$$CO\ selectivity\ (\%) = \frac{F_{out,CO}}{F_{in,CH_4}X_{CH_4} + F_{in,CO_2}X_{CO_2}} \times 100\% \quad (4)$$

$$coke\ selectivity\ (\%) = 100 - CO\ selectivity \quad (5)$$

where, X_{CH_4} and X_{CO_2} are the conversions of CH_4 and CO_2, respectively.

2.5. Temperature-Programmed Surface Reaction (TPSR)

TPSR experiments were conducted to probe the surface reaction behavior of the catalysts. The tests were carried out on a fixed-bed quartz flow reactor (inner diameter: 8 mm) loaded with 100 mg of catalyst mixed with 600 mg of quartz sand. Prior to each run, the catalyst was reduced in 10% H_2/Ar (50 $mL \cdot min^{-1}$) at 700 °C for 1 h. Three consecutive programs were performed. For CH_4-TPSR: after reduction, the bed was cooled to 100 °C under Ar (50 $mL \cdot min^{-1}$), then switched to 10% CH_4/Ar (30 $mL \cdot min^{-1}$). Once the baseline stabilized, the temperature was ramped from 100 to 850 °C with a heating rate of 10 $°C \cdot min^{-1}$. The effluent was continuously analyzed by an online mass spectrometer (GSD350 OmniStar, Pfeiffer Vacuum GmbH, Asslar, Germany), monitoring H_2 (*m*/*z* = 2), CH_4 (*m*/*z* = 16), CO (*m*/*z* = 28), and CO_2 (*m*/*z* = 44). CO_2-TPSR: after CH_4-TPSR, the reactor was purged with Ar (30 $mL \cdot min^{-1}$) and cooled to 100 °C, then fed with CO_2 (40 $mL \cdot min^{-1}$). After stabilization, the temperature was increased from 100 to 850 °C (10 $°C \cdot min^{-1}$), with the online MS detection for the effluent CO_2 and CO. CH_4&CO_2-TPSR: following CO_2-TPSR, the bed was purged with Ar and cooled to 100 °C. The mixture of CH_4/CO_2 (volume ratio of 1/1, 40 $mL \cdot min^{-1}$) was introduced, and the temperature was ramped from 100 to 850 °C (10 $°C \cdot min^{-1}$) while continuously monitoring H_2, CH_4, CO, and CO_2 signals.

3. Results and Discussion

3.1. Physicochemical Properties

Figure 1a presents the XRD patterns of the $SrTiO_3$ supports synthesized by CP, HT, and SG methods. All samples exhibited the typical diffraction peaks of the perovskite $SrTiO_3$ phase (PDF#04-007-0044), and no impurity phases such as $SrCO_3$ or TiO_2 were detected, confirming the successful formation of a single-phase perovskite structure [26,28]. The hydrothermal method promoted complete crystallization and well-defined lattice ordering, while the sol-gel route yielded slightly broader peaks due to smaller and less ordered crystallites [29,30]. The CP-STO sample showed the weakest diffraction intensity, implying lower crystallinity and partial lattice disorder, which may stem from rapid nucleation and limited particle growth during precipitation. As shown in Figure 1b,c, all $SrTiO_3$ supports displayed type IV N_2 adsorption-desorption isotherms with H3-type hysteresis loops, characteristic of mesoporous materials [31]. The pore size distribution curves revealed that the average pore diameters were primarily distributed in the 10–50 nm range. Notably, the specific surface area and pore volume varied significantly with the synthesis method (Table 1): HT-STO exhibited the largest surface area (18.78 $m^2 \cdot g^{-1}$), followed by SG-STO (13.90 $m^2 \cdot g^{-1}$), whereas CP-STO possessed only 2.70 $m^2 \cdot g^{-1}$. These variations can be attributed to differences in nucleation and crystal growth behavior—slow and controlled growth under hydrothermal conditions facilitates smaller, more dispersed particles and a looser microstructure, whereas the co-precipitation route tends to produce agglomerated grains with fewer accessible pores [32,33].

Table 1. Textural properties of the perovskite supports and supported Ni catalysts.

Sample	S_{BET} (m^2/g)	V_{Pore} (cm^3/g)	Sample	S_{BET} (m^2/g)	V_{Pore} (cm^3/g)
CP-STO	2.70	0.0081	Ni/CP-STO	2.35	0.0115
HT-STO	18.78	0.1150	Ni/HT-STO	16.58	0.1085
SG-STO	13.90	0.0745	Ni/SG-STO	12.22	0.0677

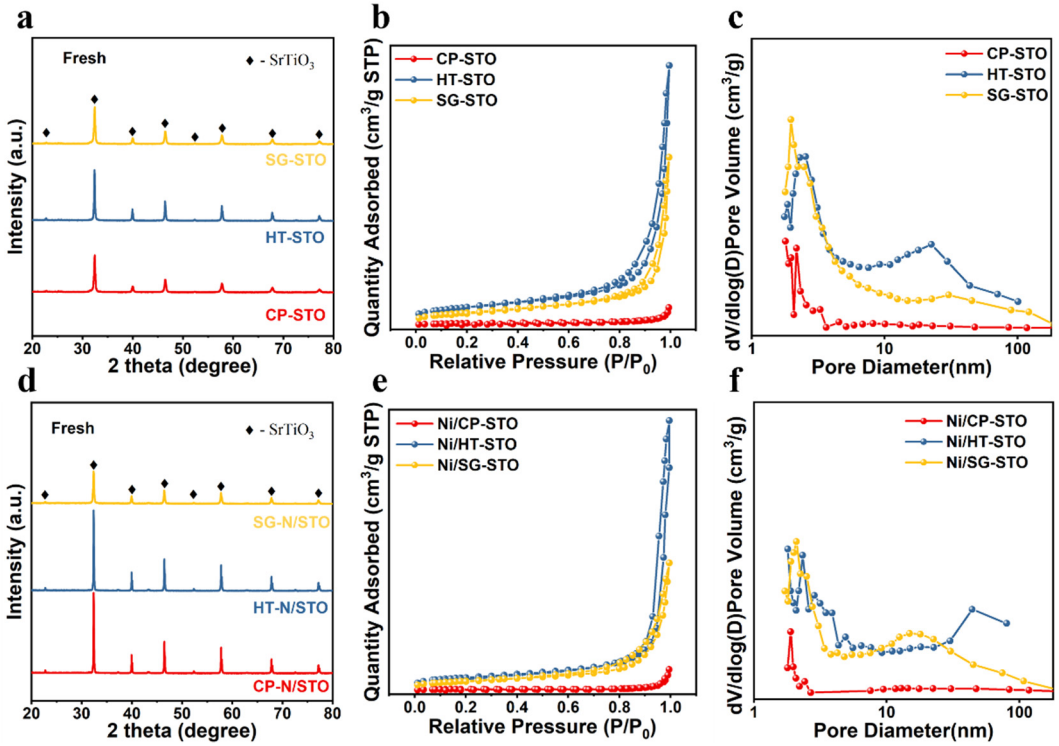

Figure 1. (**a**) XRD patterns, (**b**) N_2 adsorption-desorption isotherms, and (**c**) BJH pore-size distributions of $SrTiO_3$ supports prepared by different methods. (**d**–**f**) The corresponding results for Ni-loaded catalysts.

After Ni impregnation, the XRD patterns of the Ni/$SrTiO_3$ catalysts (Figure 1d) remained nearly identical to those of the corresponding supports, with no detectable reflections corresponding to Ni or NiO species [34]. This indicates that the Ni nanoparticles were either highly dispersed on the $SrTiO_3$ surface or partially incorporated into the perovskite lattice through substitutional sites. The preservation of the perovskite structure upon Ni loading demonstrates the excellent structural stability of $SrTiO_3$. As shown in Figure 1e,f, the N_2 isotherms and pore-size distributions of the Ni-loaded samples were consistent with those of the bare supports, suggesting that the impregnation process did not significantly alter the textural features.

Figure 2a shows the XRD patterns of the catalysts after reduction at 700 °C for 1 h. All samples maintain the characteristic diffraction peaks of $SrTiO_3$, indicating that the perovskite framework remains stable during the reduction process [35,36]. In addition, distinct reflections assigned to metallic Ni appear in each catalyst, confirming that the NiO species were successfully reduced to Ni^0. The absence of any impurity or decomposition phase demonstrates that the reduction treatment does not induce structural collapse, further evidencing the excellent thermal stability of the $SrTiO_3$ support. Notably, the diffraction peaks of Ni/SG-STO are relatively broad and weak compared with those of Ni/CP-STO and Ni/HT-STO, suggesting that the sol-gel route favors the formation of smaller Ni crystallites with higher dispersion on the surface. This trend is consistent with the quantitative results summarized in Table 2, where Ni/SG-STO exhibits the smallest Ni crystallite and particle sizes (14.6–14.9 nm from XRD/TEM) together with the highest dispersion (5.9%), whereas Ni/CP-STO and Ni/HT-STO possess larger Ni domains and lower dispersions.

Table 2. Characterization and evaluation of the employed Ni/$SrTiO_3$ catalysts.

Catalyst	Ni Crystalline Size (nm, Reduced)		Ni Crystalline Size (nm, Spent)		Ni Loading [e] (wt%)	Ni Dispersion [f] (%)
	d_1 [a]	d_2 [b]	d_1 [c]	d_2 [d]		
CP-Ni/STO	24.56	25.83	27.18	30.12	4.78	2.1
HT-Ni/STO	26.04	27.12	32.50	33.20	4.86	4.4
SG-Ni/STO	14.61	14.91	16.94	17.55	4.89	5.9

[a] Calculated using the Scherrer equation based on the Ni (111) diffraction peak in Figure 2a. [b] Obtained from the average particle size statistics based on the TEM particle size distribution data in Figure 3a–c. [c] Calculated using the Scherrer equation based on the Ni (111) diffraction peak in Figure 5a. [d] Obtained from the average particle size statistics based on the TEM particle size distribution data in Figure 7a,d,g. [e] Determined by ICP-OES. [f] Estimated by H_2 chemisorption at 50 °C.

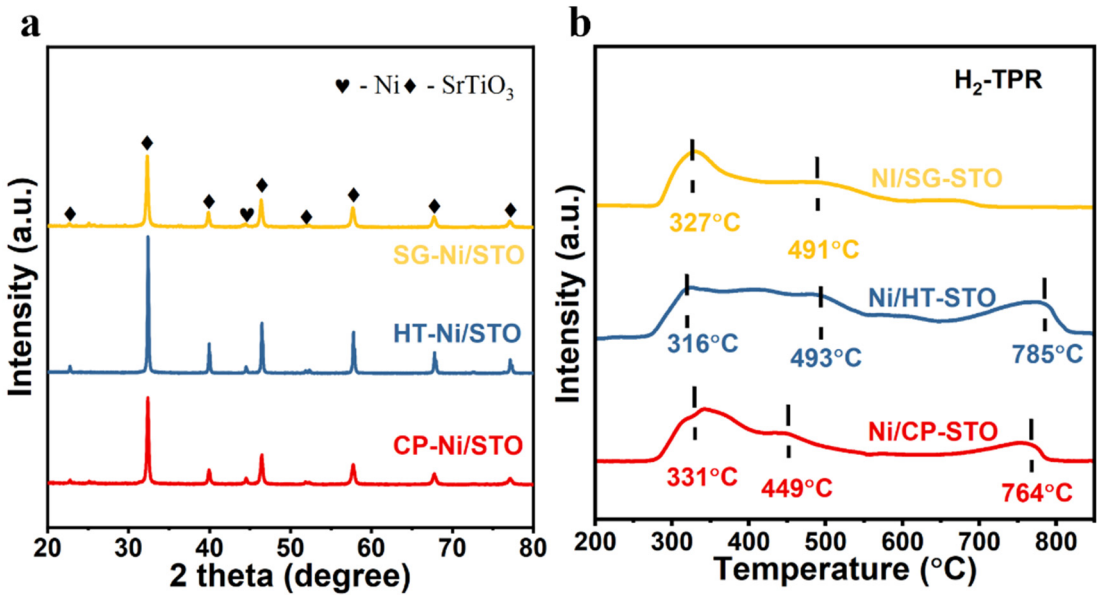

Figure 2. (**a**) XRD patterns of Ni/CP-STO, Ni/HT-STO, and Ni/SG-STO catalysts after reduction at 700 °C for 1 h; (**b**) H_2-TPR profiles of the catalysts.

The H_2-TPR profiles (Figure 2b) reveal distinct reduction behaviors among the three catalysts. Multiple reduction regions can be identified, corresponding to Ni species with different interaction strengths: surface NiO weakly bound to the support (below 350 °C), interfacial NiO-$SrTiO_3$ species (400–550 °C), and strongly incorporated Ni^{2+} in the perovskite lattice (above 700 °C) [37,38]. Both Ni/CP-STO and Ni/HT-STO exhibit three well-resolved reduction peaks, indicating the coexistence of surface NiO and lattice embedded Ni^{2+} species. In contrast, Ni/SG-STO displays two broader peaks with a less pronounced high-temperature signal, suggesting a more homogeneous Ni distribution and fewer Ni^{2+} ions deeply incorporated in the lattice. The slightly higher reduction temperatures of Ni/SG-STO compared with Ni/CP-STO imply stronger metal-support interactions, whereas the suppressed high temperature reduction indicates that only a small fraction of Ni^{2+} species remain unreduced at 700 °C. The balanced reducibility and enhanced Ni dispersion (Table 2) demonstrate that the sol-gel method produces an optimal Ni-support interaction that simultaneously promotes high dispersion and structural stability under DRM conditions.

The TEM images and corresponding particle size distributions (Figure 3a–c) show that Ni nanoparticles are uniformly dispersed on the $SrTiO_3$ support for all samples. Among them, Ni/SG-STO exhibits the smallest and most narrowly distributed Ni particles, while Ni/CP-STO and Ni/HT-STO display slightly larger and broader size distributions, consistent with the XRD Scherrer and chemisorption results summarized in Table 2. Representative TEM and EDS mapping images of the reduced Ni/SG-STO catalyst (Figure 3d–f) further confirm the homogeneous dispersion of Ni nanoparticles on the $SrTiO_3$ surface without visible aggregation. The strong spatial overlap of Sr, Ti, and Ni signals demonstrates intimate metal-support contact, which aligns well with the enhanced interfacial interaction inferred from the H_2-TPR results [39]. The surface morphology observed by SEM (Figure 3g,h) reveals densely packed yet finely dispersed spherical grains, within which Ni nanoparticles are uniformly anchored on the $SrTiO_3$ crystallites. Such uniform microstructural features are expected to expose abundant accessible active sites while simultaneously suppressing particle sintering during DRM.

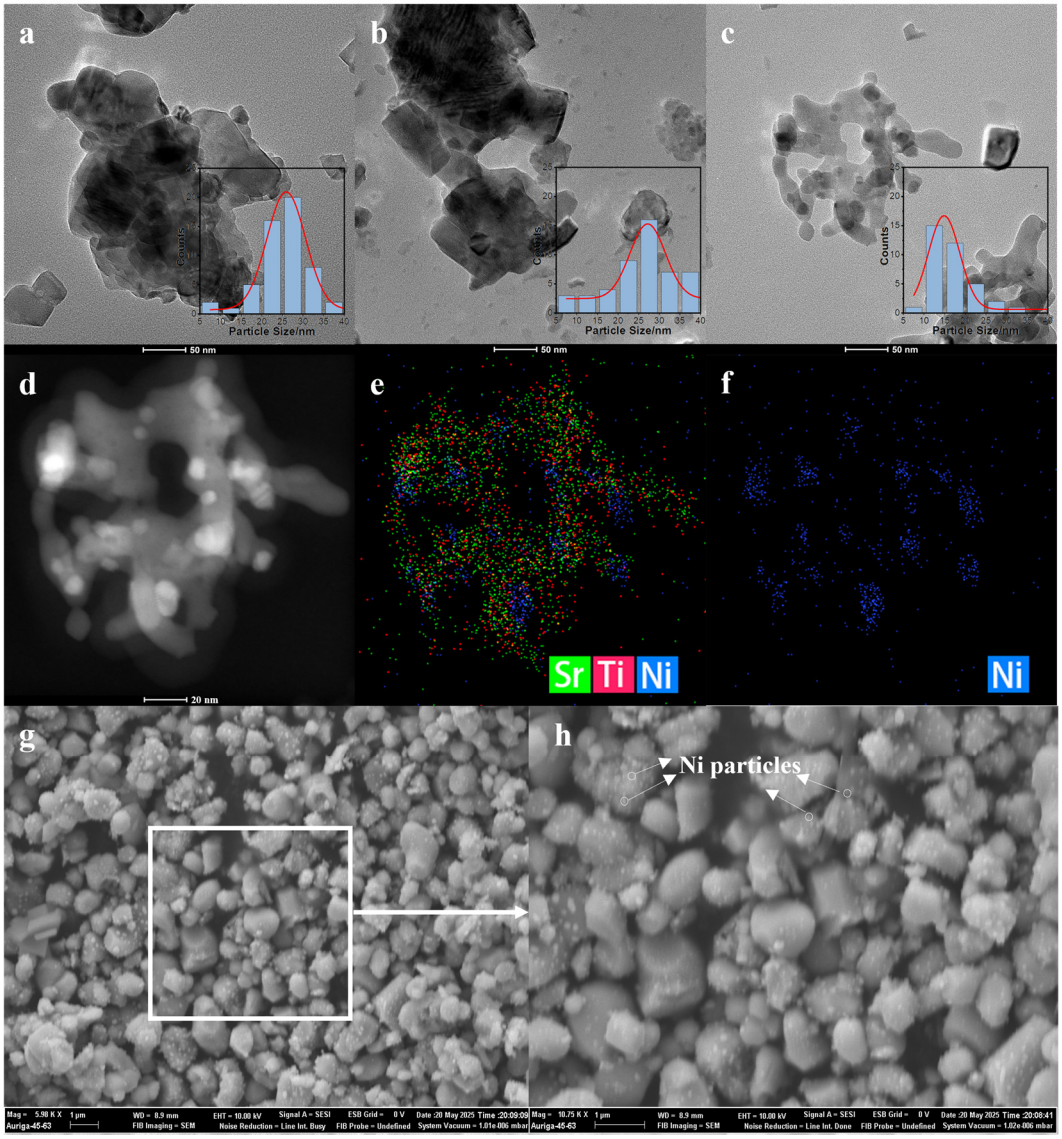

Figure 3. (**a**–**c**) TEM images and corresponding Ni particle size distributions of Ni/CP-STO, Ni/HT-STO, and Ni/SG-STO catalysts; (**d**–**f**) STEM image and the corresponding EDS elemental mappings for Ni/SG-STO; (**g**,**h**) SEM images of Ni/SG-STO. All samples were reduced in 10% H_2/Ar at 700 °C for 1 h.

3.2. Reaction Performance

Figure 4 compares the catalytic performances of Ni/CP-STO, Ni/HT-STO, and Ni/SG-STO catalysts in DRM at 700 °C. All catalysts exhibited a gradual decline in CH_4 and CO_2 conversions with time on stream, yet the extent of deactivation clearly depended on the preparation method. The initial CH_4 conversions followed the order Ni/SG-STO (68.9%) > Ni/HT-STO (66.3%) > Ni/CP-STO (44.8%), consistent with their Ni dispersion levels (5.9%, 4.4%, and 2.1%). The higher dispersion and smaller Ni crystallite size of Ni/SG-STO (14.91 nm) provided more accessible Ni^0 sites for CH_4 activation, resulting in its highest initial activity. Ni/HT-STO, with slightly larger Ni particles (27.12 nm) and weaker metal-support interaction, exhibited a comparable but slightly lower activity. In contrast, Ni/CP-STO possessed the lowest dispersion (2.1%) and the largest Ni particles (25.83 nm), leading to fewer exposed active sites and a lower CH_4 conversion.

During the 60 h stability test, the CH_4 and CO_2 conversions of all catalysts gradually decreased, but the rate of decline varied. Ni/HT-STO showed the most pronounced deactivation, indicating that its Ni particles were less strongly anchored on the support. Ni/CP-STO, despite its low initial activity, exhibited the slowest decline in conversion, which is attributed to its weaker CH_4 activation and less coke formation. Ni/SG-STO displayed intermediate behavior, combining high initial activity with acceptable stability, suggesting that the sol-gel synthesis offered a favorable balance between Ni dispersion and interaction strength [40]. The H_2/CO ratios of all catalysts were initially close to unity, confirming that the DRM reaction dominated under the tested conditions. With time on stream, the ratios gradually decreased, particularly for Ni/HT-STO, implying that the number of accessible Ni active sites decreased as the reaction

proceeded. The distinct activity and stability behaviors observed here can be rationalized by the differences in Ni dispersion and metal-support interaction derived from the synthesis method, which will be further analyzed in the following section.

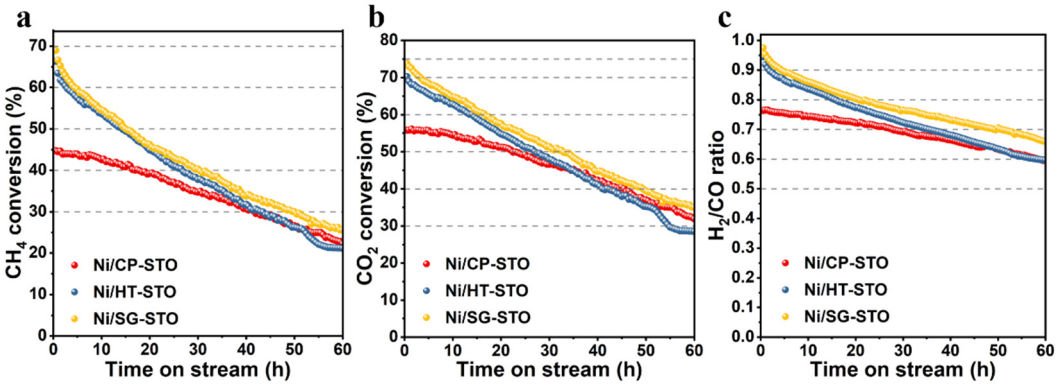

Figure 4. (**a**) CH_4 conversion, (**b**) CO_2 conversion, and (**c**) H_2/CO ratio during the DRM reaction at 700 °C over Ni/CP-STO, Ni/HT-STO, and Ni/SG-STO catalysts. The feed gas (CH_4/CO_2 = 1:1) was used without dilution, with a WHSV of 24,000 mL·g^{-1}·h^{-1}.

3.3. Sintering and Coking Analysis

Figure 5 shows the XRD patterns of the Ni/$SrTiO_3$ catalysts after the DRM reaction. All samples maintain the characteristic diffraction peaks of $SrTiO_3$, confirming that the perovskite framework remains intact even after prolonged operation at 700 °C. This excellent phase stability highlights the strong thermal robustness of $SrTiO_3$ as a support under harsh reforming conditions. A weak diffraction feature at approximately 26.2° is detected in all spent samples and is attributed to graphitic carbon formed on the catalyst surface [41]. The intensity of this peak follows the order Ni/HT-STO > Ni/SG-STO > Ni/CP-STO, implying that the hydrothermal catalyst experiences more pronounced carbon deposition, consistent with its faster deactivation trend discussed earlier. The metallic Ni peaks remain visible, and no new impurity or NiO peaks are detected, indicating that Ni species are well stabilized on the $SrTiO_3$ surface during the reaction. According to Table 2, the Ni crystallite size changes slightly after the reaction, following the order Ni/SG-STO (2.33 nm) < Ni/CP-STO (2.62 nm) < Ni/HT-STO (6.46 nm), confirming the superior sintering resistance of Ni/SG-STO.

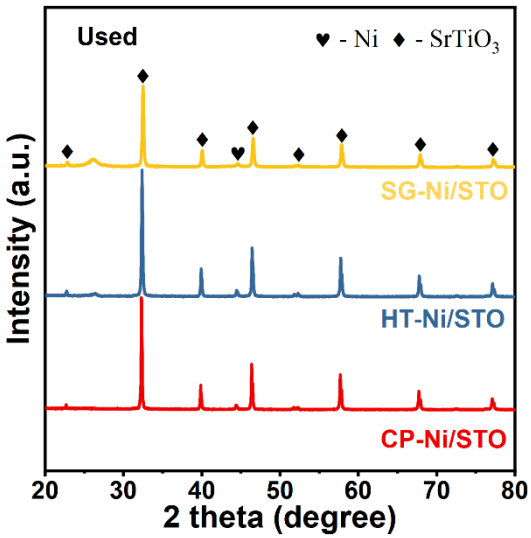

Figure 5. XRD patterns of the spent Ni/CP-STO, Ni/HT-STO, and Ni/SG-STO catalysts.

Carbon deposition behaviors were further analyzed by thermogravimetric (TG/DTG) and Raman spectroscopy in Figure 6a,b. In the TG curves measured under air flow, the total weight losses corresponding to carbon oxidation are 12.4% for Ni/HT-STO, 9.2% for Ni/SG-STO, and 7.3% for Ni/CP-STO. The DTG profiles show distinct oxidation peaks centered at approximately 640 °C for Ni/HT-STO, 605 °C for Ni/CP-STO, and 580 °C for Ni/SG-STO, respectively. The lower combustion temperature of Ni/SG-STO indicates that the deposited carbon is more reactive and easier to oxidize, whereas the higher temperature peak of Ni/HT-STO corresponds to more graphitic, strongly bound

carbon that requires higher energy for removal [42]. Notably, the smallest carbon amount on Ni/CP-STO is consistent with its relatively low activity and slower deactivation rate, since fewer active Ni sites for CH_4 dissociation generate less coke despite the lower overall performance.

As shown in Figure 6c, two characteristic bands appear at around 1350 cm^{-1} (D band, disordered amorphous carbon) and 1580 cm^{-1} (G band, graphitic carbon). The intensity ratio (I_D/I_G) reflects the degree of graphitization: a lower ratio indicates more ordered, inert carbon species, whereas a higher ratio suggests more disordered, reactive carbon [41]. The I_D/I_G ratios follow the order Ni/HT-STO (0.71) < Ni/CP-STO (0.85) ≈ Ni/SG-STO (0.86). Combining these results, the higher oxidation temperature and lower I_D/I_G ratio of Ni/HT-STO confirm that it mainly accumulates dense graphitic carbon, which is thermally stable and difficult to remove [43,44]. In contrast, the lower oxidation temperature and higher I_D/I_G ratio of Ni/SG-STO reveal that the deposited carbon is more amorphous and less ordered, consistent with its partial removal during reaction and slower deactivation rate. The Ni/CP-STO sample shows the smallest carbon amount and an intermediate oxidation temperature, reflecting its limited CH_4 dissociation activity and hence reduced carbon formation. Furthermore, as shown in Figure 6d, the coke selectivity has been calculated to evaluate the carbon formation tendency of the catalysts. Considering that carbon deposition in the DRM process mainly originates from CH_4 cracking, this calculation provides a quantitative approach to assess the catalysts' resistance to carbon accumulation. The results correspond well with the above TG analysis.

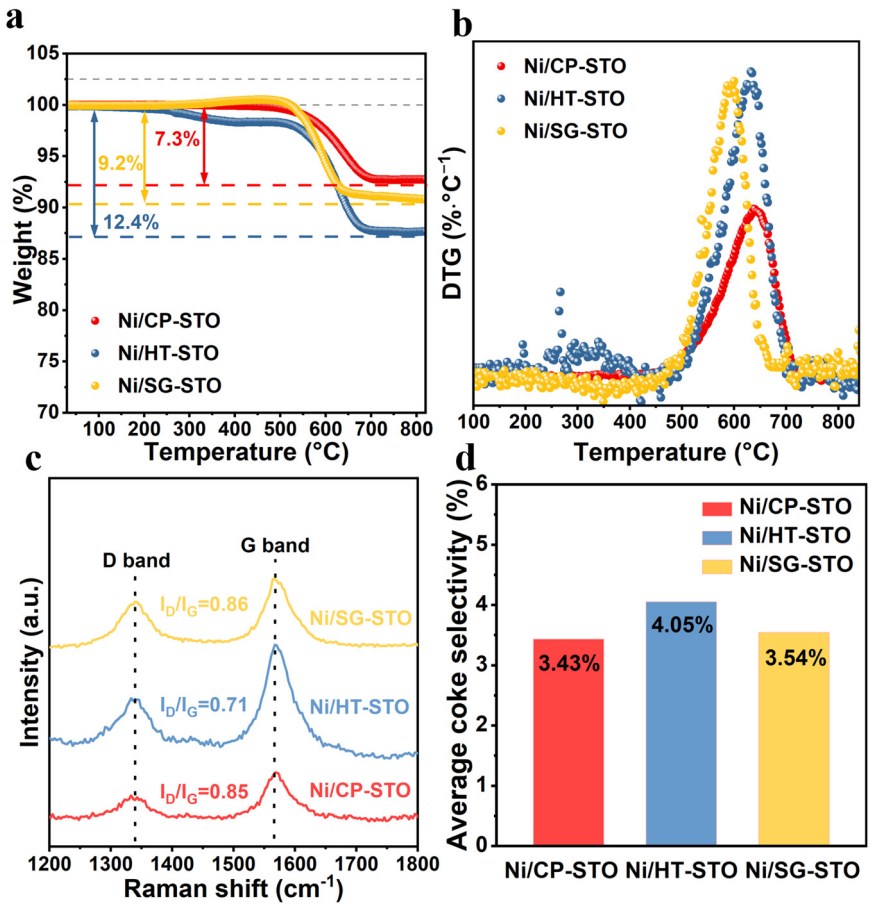

Figure 6. (**a**) TG, (**b**) DTG and (**c**) Raman spectra of the spent Ni/CP-STO, Ni/HT-STO, and Ni/SG-STO catalysts. (**d**) Coke selectivity during the DRM reaction over Ni/CP-STO, Ni/HT-STO, and Ni/SG-STO catalysts.

The TEM and EDS analyses (Figure 7) provide direct insights into the carbon deposition behavior and morphological evolution of the catalysts after the DRM reaction. All three samples exhibit the formation of filamentous carbon or carbon nanotubes surrounding the Ni particles, confirming that carbon accumulation occurs to varying extents. For Ni/CP-STO (Figure 7a–c), most Ni nanoparticles remain anchored to the $SrTiO_3$ surface with only a limited amount of carbon filaments, consistent with the lower carbon content observed in the TG results. The strong Ni-support interaction and relatively low methane activation activity of the co-precipitated catalyst effectively suppress excessive carbon growth [45–47]. In contrast, Ni/HT-STO (Figure 7d–f) shows numerous Ni nanoparticles detached from the $SrTiO_3$ surface and encapsulated by thick filamentous carbon layers. These carbon filaments grow outward from the Ni

particles, forming a network structure typical of catalytic carbon deposition, which blocks active sites and accelerates catalyst deactivation [48]. This observation agrees well with its highest weight loss in TG analysis and lowest I_D/I_G ratio in Raman spectra, both indicating the formation of graphitic, thermally stable carbon that is difficult to remove. The Ni/SG-STO catalyst (Figure 7g–i) also exhibits filamentous carbon structures, but a considerable portion of Ni nanoparticles remains in close contact with the support. According to the TEM particle size statistics summarized in Table 2, the average Ni particle size after reaction increases slightly for all catalysts, following the order Ni/SG-STO (2.7 nm) < Ni/CP-STO (4.3 nm) < Ni/HT-STO (6.1 nm). This trend clearly demonstrates that the sol-gel derived Ni/SG-STO possesses the strongest anti-sintering ability under DRM conditions.

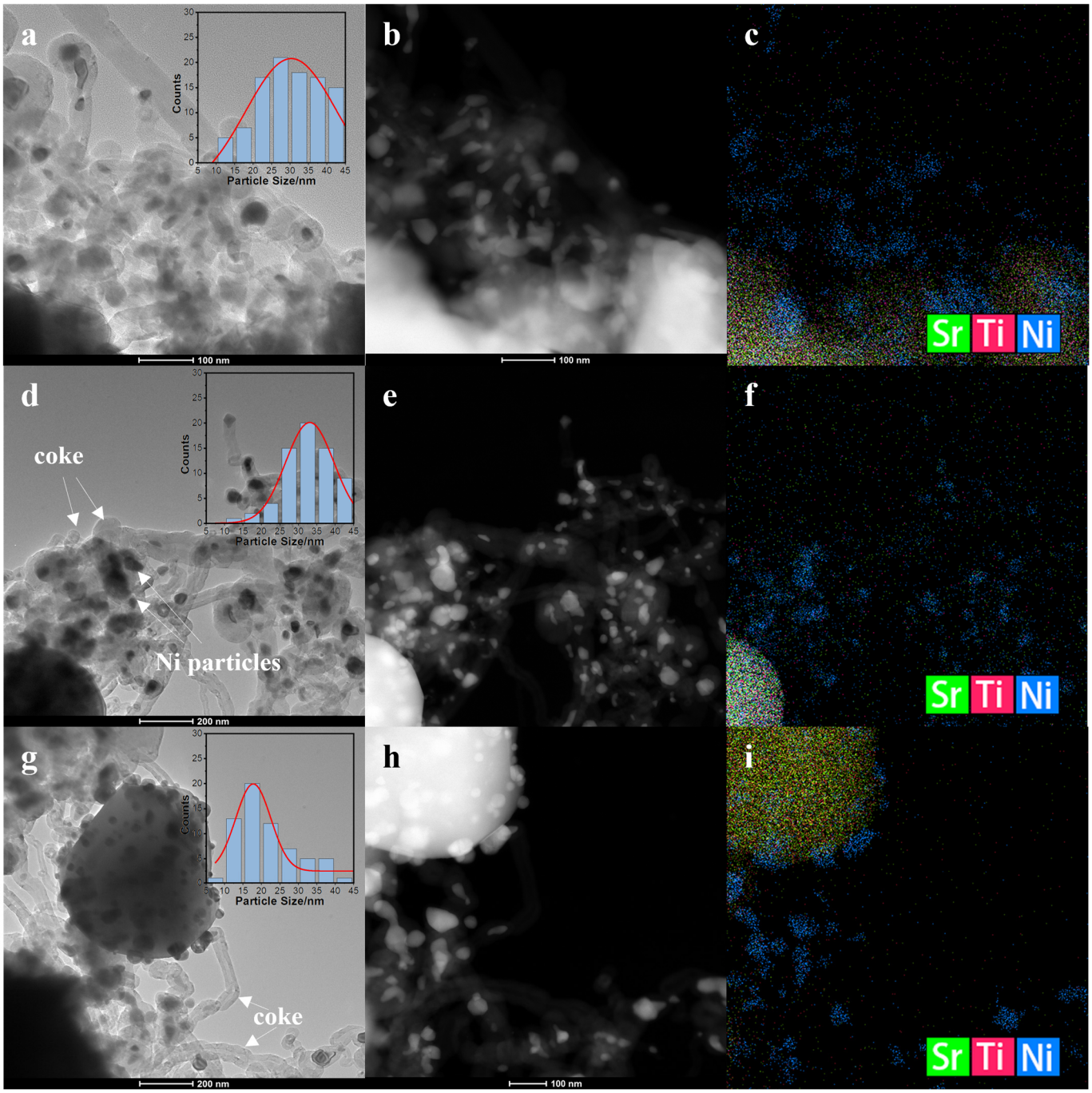

Figure 7. TEM, STEM, and corresponding EDS elemental mapping images of the spent (**a**–**c**) Ni/CP-STO, (**d**–**f**) Ni/HT-STO, and (**g**–**i**) Ni/SG-STO catalysts.

3.4. Surface Reaction Study

To gain further insight into the surface reaction behavior and the relationship between structural characteristics and catalytic performance, temperature-programmed surface reaction (TPSR) experiments were conducted over Ni/H-STO and Ni/SG-STO catalysts.

In the CH_4-TPSR profiles (Figure 8a,b), both catalysts display distinct H_2 evolution, indicating CH_4 decomposition on metallic Ni sites. For Ni/H-STO, the H_2 signal emerges at around 300 °C and increases sharply with temperature, reflecting a strong CH_4 activation ability. However, a temporary decline occurs near 600 °C, followed by a new rise above 700 °C, which can be attributed to the blockage of Ni sites by accumulated carbon at intermediate temperatures and subsequent partial carbon removal at higher temperatures. In contrast, Ni/SG-STO initiates H_2 formation at a higher temperature (≈420 °C), implying that its stronger Ni-support interaction slightly retards CH_4 dissociation [35,49]. Nevertheless, its H_2 evolution remains smoother and more stable throughout the heating process, suggesting suppressed carbon accumulation and better Ni stabilization.

The CO_2-TPSR curves (Figure 8c,d) reveal distinct CO_2 activation behaviors. Ni/H-STO exhibits a weak CO signal at 533 °C, indicating limited CO_2 dissociation and slow carbon oxidation. Conversely, Ni/SG-STO shows CO generation beginning at 524 °C and peaking near 630 °C, confirming the enhanced CO_2 activation. Higher CO intensity implies that CO_2 molecules can more effectively interact with surface carbon and lattice oxygen, facilitating carbon removal [50,51]. During the CH_4&CO_2-TPSR process (Figure 8e,f), Ni/SG-STO exhibits simultaneous H_2 and CO release at lower temperatures (504–539 °C) compared to Ni/H-STO (521–568 °C), indicating that both CH_4 and CO_2 activation proceed more readily. The concurrent evolution of H_2 and CO suggests a well-coupled reforming mechanism, where CH_4 decomposition and CO_2 reduction are dynamically balanced [52,53]. Overall, these results reveal a clear structure activity correlation: the sol-gel derived Ni/SG-STO possesses an optimal Ni-support interaction and higher interfacial oxygen mobility, enabling more efficient CO_2 activation and continuous carbon removal. In contrast, the weaker interfacial bonding in Ni/H-STO promotes faster CH_4 dissociation but also severe carbon buildup, leading to periodic site blockage and faster deactivation.

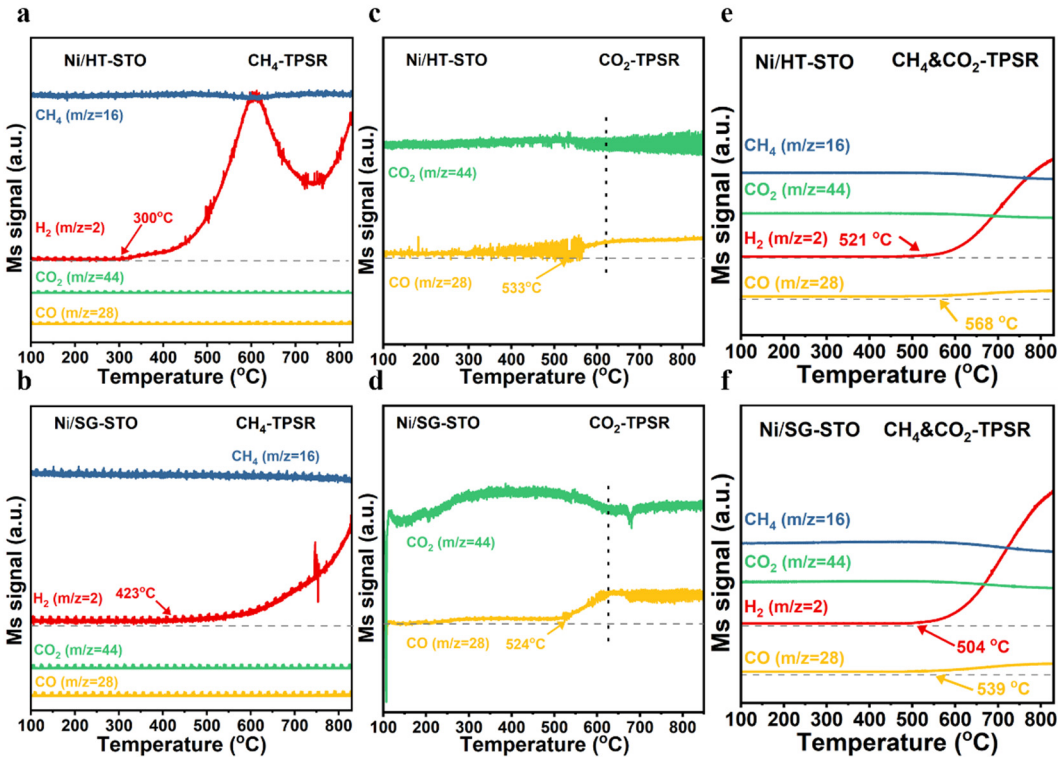

Figure 8. (**a**,**b**) CH_4-TPSR, (**c**,**d**) CO_2-TPSR, and (**e**,**f**) CH_4&CO_2-TPSR profiles of Ni/HT-STO and Ni/SG-STO catalysts.

4. Conclusions

This study systematically investigated Ni/$SrTiO_3$ catalysts prepared by CP, HT, and SG methods to elucidate the influence of preparation routes on the structure-performance relationship in DRM. All catalysts retained the perovskite $SrTiO_3$ structure after reduction and reaction, confirming the excellent thermal stability of the support. Among them, HT-STO and SG-STO exhibited larger surface areas (18.78 and 13.90 $m^2 \cdot g^{-1}$) than CP-STO (2.70 $m^2 \cdot g^{-1}$). The Ni/SG-STO catalyst possessed the smallest Ni crystallite size (14.91 nm) and the highest Ni dispersion (5.9%), while Ni/HT-STO showed a slightly larger Ni size (27.12 nm) but still higher dispersion (4.4%) than Ni/CP-STO (25.83 nm, 2.1%). These structural features contributed to their higher initial CH_4 conversions of 66.3% and 68.9%, respectively, compared

with 44.8% for Ni/CP-STO. However, Ni/HT-STO showed the fastest deactivation, with CH_4 conversion dropping to 21.2% after 60 h due to severe carbon deposition (12.4 wt%) and pronounced Ni sintering (particle growth of 6.08 nm). In contrast, Ni/SG-STO maintained higher activity (25.6% after 60 h) with moderate carbon accumulation (9.2 wt%) and minimal Ni particle growth (2.64 nm), confirming its strong resistance to sintering and coking. Raman and TG-DTG analyses further revealed that Ni/SG-STO mainly formed less graphitic, more reactive carbon species, whereas Ni/HT-STO accumulated dense graphitic carbon that was difficult to remove. TPSR results also indicated that Ni/SG-STO enabled CH_4 activation and CO_2 dissociation to occur at lower temperatures (504 °C and 539 °C), achieving better carbon-oxygen coupling and continuous surface renewal. Overall, these results demonstrate that the sol-gel route provides a favorable balance between Ni dispersion and interfacial bonding, effectively enhancing the anti-sintering, anti-coking, and reaction-coupling performance of Ni/$SrTiO_3$ catalysts under DRM conditions.

Author Contributions

Conceptualization, T.Y. and M.Z.; Methodology, T.Y. and H.S.; Formal Analysis, T.Y.; Investigation, T.Y., H.S. and N.J.; Validation, H.S. and J.Y.; Data Curation, T.Y.; Visualization, T.Y.; Writing—Original Draft Preparation, T.Y.; Writing—Review & Editing, M.Z. and J.Y.; Supervision, M.Z.; Project Administration, M.Z.; Funding Acquisition, M.Z.

Ethics Statement

Not applicable.

Informed Consent Statement

Not applicable.

Data Availability Statement

Data will be made available on request.

Funding

This research was funded by the National Natural Science Foundation of China (Grant No. 22408348) and the Natural Science Foundation of Henan Province, China (Grant No. 242300421599).

Declaration of Competing Interest

The authors declare that they have no known competing financial interests or personal relationships that could have appeared to influence the work reported in this paper.

References

1. Welsby D, Price J, Pye S, Ekins P. Unextractable Fossil Fuels in a 1.5 °C World. *Nature* **2021**, *597*, 230–234. doi:10.1038/s41586-021-03821-8.
2. Yang R, He C, Dong Y, Chen W, Chen L, Wang Z, et al. Photothermal Methane Dry Reforming: Catalyst Architectures, Mechanistic Pathways, and Future Challenges. *Chem. Soc. Rev.* **2025**, *54*, *in press*. doi:10.1039/d5cs00417a.
3. Zhang G, Liu J, Xu Y, Sun Y. A Review of CH_4/CO_2 Reforming to Synthesis Gas over Ni-Based Catalysts in Recent Years (2010–2017). *Int. J. Hydrogen Energy* **2018**, *43*, 15030–15054. doi:10.1016/j.ijhydene.2018.06.091.
4. He C, Li Q, Ye Z, Wang L, Gong Y, Li S, et al. Regulating Atomically-Precise Pt Sites for Boosting Light-Driven Dry Reforming of Methane. *Angew. Chem. Int. Ed.* **2024**, *63*, e202412308. doi:10.1002/anie.202412308.
5. Awad MM, Hussain I, Mustapha U, Ahmed Taialla O, Musa Alhassan A, Kotob E, et al. A Critical Review of Recent Advancements in Catalytic Dry Reforming of Methane: Physicochemical Properties, Current Challenges, and Informetric Insights. *Int. J. Hydrogen Energy* **2024**, *76*, 202–233. doi:10.1016/j.ijhydene.2024.03.319.
6. Overa S, Ko BH, Zhao Y, Jiao F. Electrochemical Approaches for CO_2 Conversion to Chemicals: A Journey toward Practical Applications. *Acc. Chem. Res.* **2022**, *55*, 638–648. doi:10.1021/acs.accounts.1c00674.
7. He C, Wu S, Li Q, Li M, Li J, Wang L, et al. Constructing Matched Active Sites for Robust Photocatalytic Dry Reforming of Methane. *Chem* **2023**, *9*, 3224–3244. doi:10.1016/j.chempr.2023.06.021.
8. Gao P, Li S, Bu X, Dang S, Liu Z, Wang H, et al. Direct Conversion of CO_2 into Liquid Fuels with High Selectivity over a Bifunctional Catalyst. *Nat. Chem.* **2017**, *9*, 1019–1024. doi:10.1038/nchem.2794.

9. Cheng K, Gu B, Liu X, Kang J, Zhang Q, Wang Y. Direct and Highly Selective Conversion of Synthesis Gas into Lower Olefins: Design of a Bifunctional Catalyst Combining Methanol Synthesis and Carbon–Carbon Coupling. *Angew. Chem. Int. Ed.* **2016**, *55*, 4725–4728. doi:10.1002/anie.201601208.
10. Wang J, Li R, Zhang G, Dong C, Fan Y, Yang S, et al. Confinement-Induced Indium Oxide Nanolayers Formed on Oxide Support for Enhanced CO_2 Hydrogenation Reaction. *J. Am. Chem. Soc.* **2024**, *146*, 5523–5531. doi:10.1021/jacs.3c13355.
11. Royer S, Duprez D, Can F, Courtois X, Batiot-Dupeyrat C, Laassiri S, et al. Perovskites as Substitutes of Noble Metals for Heterogeneous Catalysis: Dream or Reality. *Chem. Rev.* **2014**, *114*, 10292–10368. doi:10.1021/cr500032a.
12. Wang Y, Li R, Zeng C, Sun W, Fan H, Ma Q, et al. Recent research progress of methane dry reforming to syngas. *Fuel* **2025**, *398*, 135535. doi:10.1016/j.fuel.2025.135535.
13. Wang J, Kalaev D, Yang J, Waluyo I, Hunt A, Sadowski JT, et al. Fast Surface Oxygen Release Kinetics Accelerate Nanoparticle Exsolution in Perovskite Oxides. *J. Am. Chem. Soc.* **2023**, *145*, 1714–1727. doi:10.1021/jacs.2c10256.
14. Paksoy AI, Caglayan BS, Aksoylu AE. An *In Situ* FTIR-DRIFTS Study on CDRM over Co–Ce/ZrO_2: Active Surfaces and Mechanistic Features. *Int. J. Hydrogen Energy* **2020**, *45*, 12822–12834. doi:10.1016/j.ijhydene.2020.03.012.
15. Alves LMNC, Almeida MP, Ayala M, Watson CD, Jacobs G, Rabelo-Neto RC, et al. CO_2 Methanation over Metal Catalysts Supported on ZrO_2: Effect of the Nature of the Metallic Phase on Catalytic Performance. *Chem. Eng. Sci.* **2021**, *239*, 116604. doi:10.1016/j.ces.2021.116604.
16. Ma L, Ye R, Huang Y, Reina TR, Wang X, Li C, et al. Enhanced Low-Temperature CO_2 Methanation Performance of Ni/ZrO_2 Catalysts via a Phase Engineering Strategy. *Chem. Eng. J.* **2022**, *446 Pt 2*, 137031. doi:10.1016/j.cej.2022.137031.
17. Bhattar S, Abedin MA, Kanitkar S, Spivey JJ. A Review on Dry Reforming of Methane over Perovskite Derived Catalysts. *Catal. Today* **2021**, *365*, 2–23. doi:10.1016/j.cattod.2020.10.041.
18. Georgiadis AG, Charisiou ND, Goula MA. A Mini-Review on Lanthanum–Nickel-Based Perovskite-Derived Catalysts for Hydrogen Production via the Dry Reforming of Methane (DRM). *Catalysts* **2023**, *13*, 1357. doi:10.3390/catal13101357.
19. Jeong H, Kim YH, Won B-R, Jeon H, Park C, Myung J. Emerging Exsolution Materials for Diverse Energy Applications: Design, Mechanism, and Future Prospects. *Chem. Mater.* **2023**, *35*, 3745–3764. doi:10.1021/acs.chemmater.3c00004.
20. Li Y, Chen M, Jiang L, Tian D, Li K. Perovskites as Oxygen Storage Materials for Chemical Looping Partial Oxidation and Reforming of Methane. *Phys. Chem. Chem. Phys.* **2024**, *26*, 1516–1540. doi:10.1039/D3CP04626E.
21. Li H, Tang Y, Yan W, Liu M, Wang Z, Li J, et al. Vacancy-Enhanced Photothermal Activation for CO_2 Methanation on Ni/$SrTiO_3$ Catalysts. *Appl. Catal. B* **2024**, *357*, 124346. doi:10.1016/j.apcatb.2024.124346.
22. Luo Z, Yang F, Zhang S, He G, Du C, Zhang L, et al. Engineering Crystalline Facets to Boost the Performance of Ru/$SrTiO_3$ in Photo-Thermal Coupling Hydrogenation of CO_2. *Appl. Catal. B* **2025**, *375*, 125397. doi:10.1016/j.apcatb.2025.125397.
23. Cao D, Luo C, Luo T, Shi Z, Wu F, Li X, et al. Dry Reforming of Methane by La_2NiO_4 Perovskite Oxide, Part I: Preparation and Characterization of the Samples. *Fuel Process. Technol.* **2023**, *247*, 107765. doi:10.1016/j.fuproc.2023.107765.
24. Pirzadi Z, Meshkani F. Preparation of a Nanostructured Ni/$CaO{\cdot}Al_2O_3$ Catalyst for Syngas Production via Glycerol Dry Reforming: Role of the Preparation Method. *Ind. Eng. Chem. Res.* **2024**, *63*, 6562–6576. doi:10.1021/acs.iecr.3c04288.
25. Cao D, Luo C, Cai G, Luo T, Wu F, Li X, et al. Development and Regeneration Performance of $LaNiO_3$ Perovskite Oxides for Dry Reforming of Methane. *J. Therm. Sci.* **2023**, *32*, 1935–1944. doi:10.1007/s11630-023-1849-0.
26. Suárez-Vázquez SI, Gil S, García-Vargas JM, Cruz-López A, Giroir-Fendler A. Catalytic Oxidation of Toluene by $SrTi_{1-x}B_xO_3$ (B = Cu and Mn) with Dendritic Morphology Synthesized by One-Pot Hydrothermal Route. *Appl. Catal. B* **2018**, *223*, 201–208. doi:10.1016/j.apcatb.2017.04.042.
27. Sunny MA, Gouadria S, Javed R, Iqbal MW, Zeeshan M, Ashraf M, et al. Synthesis and Characterizations of Dual Functional MOF-74/$SrTiO_3$ Composite for Next Generation Energy Storage and Hydrogen Evolution Technologies. *Mater. Today Chem.* **2025**, *48*, 102938. doi:10.1016/j.mtchem.2025.102938.
28. Liu Y, Wang X, Wang Z, Chen C, Song J, Zhang L, et al. Hydrogenation of CO_2 to CH_3OH on the Cu–ZnO–$SrTiO_3$ Catalysts: The Electronic Metal–Support Interaction Induces Oxygen Vacancy Generation. *ACS Catal.* **2024**, *14*, 12610–12622. doi:10.1021/acscatal.4c02289.
29. Shin SA, Alizadeh Eslami A, Noh YS, Song H, Kim HD, Ghaffari Saeidabad N, et al. Preparation and Characterization of Ni/$ZrTiAlO_x$ Catalyst via Sol-Gel and Impregnation Methods for Low-Temperature Dry Reforming of Methane. *Catalysts* **2020**, *10*, 1335. doi:10.3390/catal10111335.
30. Peng C, Wang L, Yu D, Zhao Z, Yu X. Research Progress of the Preparation of Perovskite Oxide Catalysts and Their Catalytic Performances for Soot Combustion. *Sci. Sin. Chim.* **2020**, *50*, 1816–1835. doi:10.1360/SSC-2020-0062.
31. Jiang K, Zhou X, Gao Y, Yang T, Zhang M, Xu Z, et al. CO_2 Methanation over Ru Catalysts: Support Engineering on the Induction Period via Tuning Metal–Support Interaction. *Fuel* **2025**, *397*, 135413. doi:10.1016/j.fuel.2025.135413.
32. Phoon BL, Lai CW, Juan JC, Show P, Chen W. A Review of Synthesis and Morphology of $SrTiO_3$ for Energy and Other Applications. *Int. J. Energy Res.* **2019**, *43*, 5151–5174. doi:10.1002/er.4505.
33. Shi Y, Tian X, Deng Z, Shi W, Fan W, Wang F. Review and Outlook of Confined Ni Catalysts for the Dry Reforming of Methane Reaction. *Energy Fuels* **2024**, *38*, 1633–1656. doi:10.1021/acs.energyfuels.3c03923.

34. Joo S, Seong A, Kwon O, Kim K, Lee JH, Gorte RJ, et al. Highly Active Dry Methane Reforming Catalysts with Boosted in Situ Grown Ni–Fe Nanoparticles on Perovskite via Atomic Layer Deposition. *Sci. Adv.* **2020**, *6*, eabb1573. doi:10.1126/sciadv.abb1573.
35. Ding X, Yang Y, Li Z, Huang P, Liu X, Guo Y, et al. Engineering a Nickel–Oxygen Vacancy Interface for Enhanced Dry Reforming of Methane: A Promoted Effect of CeO_2 Introduction into Ni/MgO. *ACS Catal.* **2023**, *13*, 15535–15545. doi:10.1021/acscatal.3c04150.
36. Bian Z, Wang Z, Jiang B, Hongmanorom P, Zhong W, Kawi S. A Review on Perovskite Catalysts for Reforming of Methane to Hydrogen Production. *Renew. Sustain. Energy Rev.* **2020**, *134*, 110291. doi:10.1016/j.rser.2020.110291.
37. Zhang M, Zhang J, Wu Y, Pan J, Zhang Q, Tan Y, et al. Insight into the Effects of the Oxygen Species over Ni/ZrO_2 Catalyst Surface on Methane Reforming with Carbon Dioxide. *Appl. Catal. B* **2019**, *244*, 427–437. doi:10.1016/j.apcatb.2018.11.068.
38. Zhu Q, Cheng H, Zou X, Lu X, Xu Q, Zhou Z. Synthesis, Characterization, and Catalytic Performance of $La_{0.6}Sr_{0.4}Ni_xCo_{1-x}O_3$ Perovskite Catalysts in Dry Reforming of Coke Oven Gas. *Chin. J. Catal.* **2015**, *36*, 915–924. doi:10.1016/S1872-2067(14)60303-X.
39. Wang Y, Sun X, Yu X, Zhang R, Yan B. Coke-Resistant $NdFe_{0.7}Ni_{0.3}O_3$ Perovskite Catalyst with Superior Stability for Dry Reforming of Ethane. *Appl. Catal. B* **2023**, *337*, 123010. doi:10.1016/j.apcatb.2023.123010.
40. Zhang M, Zhou X, Yang J, Yang T, Liu Z, Han Y. Deciphering the ZrO_2 Phase Engineering Effects on Dry Reforming of Methane over the Ni/ZrO_2 Catalysts. *Fuel* **2023**, *349*, 128705. doi:10.1016/j.fuel.2023.128705.
41. Wang Z, Li J, Wang Y, Zhang R, Liu X, Wang G, et al. Unraveling the Effects of Ce/Zr Molar Ratio in Mesoporous $Ce_xZr_{1-x}O_2$ on the Performance of Dry Reforming of Methane over Supported Ni Catalysts. *Fuel Process. Technol.* **2023**, *247*, 107772. doi:10.1016/j.fuproc.2023.107772.
42. Shen D, Wang J, Bai Y, Lyu S, Zhang Y, Li J, et al. Carbon-Confined Ni Based Catalyst by Auto-Reduction for Low-Temperature Dry Reforming of Methane. *Fuel* **2023**, *339*, 127409. doi:10.1016/j.fuel.2023.127409.
43. Liu X, Wen J, Xie Y, Li Z, Zhong M, Nie R, et al. Modulating Proportion of Ni^0 Species Stabilized by Ni^{2+} on Ni–MgO Catalyst with Superior Stability for Dry Reforming of Methane. *Chem. Eng. J.* **2024**, *493*, 152499. doi:10.1016/j.cej.2024.152499.
44. Zheng J, Impeng S, Liu J, Deng J, Zhang D. Mo Promoting Ni-Based Catalysts Confined by Halloysite Nanotubes for Dry Reforming of Methane: Insight of Coking and H_2S Poisoning Resistance. *Appl. Catal. B* **2024**, *342*, 123369. doi:10.1016/j.apcatb.2023.123369.
45. Zhang M, Yang T, Jiang K, Gao Y, Yang J, Liu Z, et al. Rationally Constructing Metastable ZrO_2 Supported Ni Catalysts for Highly Efficient and Stable Dry Reforming of Methane. *Appl. Catal. B* **2024**, *353*, 124102. doi:10.1016/j.apcatb.2024.124102.
46. Akri M, Zhao S, Li X, Zang K, Lee AF, Isaacs MA, et al. Atomically Dispersed Nickel as Coke-Resistant Active Sites for Methane Dry Reforming. *Nat. Commun.* **2019**, *10*, 5181. doi:10.1038/s41467-019-12843-w.
47. Kim YH, Kang Y, Jo S, Jeong H, Neagu D, Myung J. Shape-Shifting Nanoparticles on a Perovskite Oxide for Highly Stable and Active Heterogeneous Catalysis. *Chem. Eng. J.* **2022**, *441*, 136025. doi:10.1016/j.cej.2022.136025.
48. Li M, Van Veen AC. Tuning the Catalytic Performance of Ni-Catalysed Dry Reforming of Methane and Carbon Deposition via Ni–CeO_2 Interaction. *Appl. Catal. B* **2018**, *237*, 641–648. doi:10.1016/j.apcatb.2018.06.032.
49. Jia Y, Wu S, Qiu P, Meng L, Zhu T. Atomically Dispersed Metal Catalysts for Methane Dry Reforming. *J. Mater. Chem. A* **2025**, *13*, 5530–5545. doi:10.1039/D4TA06970F.
50. Zhang S, Tang L, Yu J, Zhan W, Wang L, Guo Y, et al. Spherical Ni Nanoparticles Supported by Nanosheet-Assembled Al_2O_3 for Dry Reforming of CH_4: Elucidating the Induction Period and Its Excellent Resistance to Coking. *ACS Appl. Mater. Interfaces* **2021**, *13*, 58605–58618. doi:10.1021/acsami.1c17890.
51. Li Y, Wang Q, Cao M, Li S, Song Z, Qiu L, et al. Structural Evolution of Robust Ni_3Fe_1 Alloy on Al_2O_3 in Dry Reforming of Methane: Effect of Iron-Surplus Strategy from Ni_1Fe_1 to Ni_3Fe_1. *Appl. Catal. B* **2023**, *331*, 122669. doi:10.1016/j.apcatb.2023.122669.
52. Zhang M, Zhang J, Zhou Z, Chen S, Zhang T, Song F, et al. Effects of the Surface Adsorbed Oxygen Species Tuned by Rare-Earth Metal Doping on Dry Reforming of Methane over Ni/ZrO_2 Catalyst. *Appl. Catal. B* **2020**, *264*, 118522. doi:10.1016/j.apcatb.2019.118522.
53. de Lira Lima DC, Lemos IP, Gomes RS, Simplício Rodrigues LMT, Fréty RT, Resini C, et al. Study of $LaNi_{1-x}Co_xO_3$ Perovskite-Type Oxides Either Pure or Mixed with SiO_2 as Catalytic Precursors Applied in CH_4 Dry Reforming. *Catal. Lett.* **2023**, *153*, 2137–2148. doi:10.1007/s10562-022-04127-8.